ARL-TR-10292 ● FEB 2026

DEVCOM ARMY RESEARCH LABORATORY

Synergistic Ni-Ru Catalysts Supported on Gd-Doped CeO_2 for Enhanced Hydrogen Production and Coke-Resistant Ethanol Partial Oxidation

by Gene Yang, Jiangtian Li, and Deryn Chu

NOTICES

Disclaimers

The findings in this report are not to be construed as an official Department of the Army position unless so designated by other authorized documents.

Citation of manufacturer's or trade names does not constitute an official endorsement or approval of the use thereof.

Destroy this report when it is no longer needed. Do not return it to the originator.

ARL-TR-10292 ● FEB 2026

Synergistic Ni-Ru Catalysts Supported on Gd-Doped CeO_2 for Enhanced Hydrogen Production and Coke-Resistant Ethanol Partial Oxidation

Gene Yang and Jiangtian Li
Oak Ridge Associated Universities

Deryn Chu
DEVCOM Army Research Laboratory

REPORT DOCUMENTATION PAGE

1. REPORT DATE	2. REPORT TYPE	3. DATES COVERED	
		START DATE	END DATE
February 2026	Technical Report	February 2024	February 2026

4. TITLE AND SUBTITLE
Synergistic Ni-Ru Catalysts Supported on Gd-Doped CeO_2 for Enhanced Hydrogen Production and Coke-Resistant Ethanol Partial Oxidation

5a. CONTRACT NUMBER	5b. GRANT NUMBER	5c. PROGRAM ELEMENT NUMBER
W911NF-24-2-0079		
5d. PROJECT NUMBER	**5e. TASK NUMBER**	**5f. WORK UNIT NUMBER**

6. AUTHOR(S)
Gene Yang, Jiangtian Li, and Deryn Chu

7. PERFORMING ORGANIZATION NAME(S) AND ADDRESS(ES)	8. PERFORMING ORGANIZATION REPORT NUMBER
DEVCOM Army Research Laboratory ATTN: FCDD-RLA-GC Adelphi, MD 20783	ARL-TR-10292

9. SPONSORING/MONITORING AGENCY NAME(S) AND ADDRESS(ES)	10. SPONSOR/MONITOR'S ACRONYM(S)	11. SPONSOR/MONITOR'S REPORT NUMBER(S)

12. DISTRIBUTION/AVAILABILITY STATEMENT
DISTRIBUTION STATEMENT A. Approved for public release: distribution unlimited.

13. SUPPLEMENTARY NOTES

14. ABSTRACT
Hydrogen production via catalytic partial oxidation (CPOX) of ethanol is a promising approach for compact, on-demand hydrogen generation systems. Nickel (Ni)-based catalysts are widely used due to their cost-effectiveness and high activity; however, their durability is limited by coke formation and deactivation. This study investigates the role of oxygen-vacancy-rich Gd-doped ceria (GDC) as a functional support and its combined interaction with ruthenium (Ru) in Ni-based catalysts. The optimized Ni/Ru(9:1)-GDC catalyst exhibited high hydrogen yield, suppressed methane and light hydrocarbon formation, and sustained long-term stability, which was attributed to the cooperative interaction among Ni, Ru, and the oxygen-vacancy-rich GDC support. In this system, Ni provided active sites for ethanol reforming, Ru facilitated hydrogen spillover and promoted water-assisted redox processes, and the GDC support supplied mobile lattice oxygen that enabled continuous carbon removal and redox cycling. These results demonstrated the importance of tuning metal-support interactions and exploiting redox-active oxide supports in the design of durable and efficient CPOX catalysts, providing practical design insights for distributed hydrogen generation applications.

15. SUBJECT TERMS
ethanol reformation, catalytic partial oxidation, hydrogen production, bimetallic catalyst, oxygen vacancies, coke resistance, Energy Sciences

16. SECURITY CLASSIFICATION OF:			17. LIMITATION OF ABSTRACT	18. NUMBER OF PAGES
a. REPORT	b. ABSTRACT	C. THIS PAGE		
UNCLASSIFIED	UNCLASSIFIED	UNCLASSIFIED	UU	30

19a. NAME OF RESPONSIBLE PERSON	19b. PHONE NUMBER *(Include area code)*
Gene Yang	(520) 691-5579

STANDARD FORM 298 (REV. 5/2020)
Prescribed by ANSI Std. Z39.18

Contents

List of Figures

List of Tables

1. Introduction

As defense and field-operable energy systems increasingly require resilient and deployable hydrogen production capabilities, the development of efficient and durable catalysts for hydrocarbon fuel reforming has become a critical technical need.[1–3] Ethanol has emerged as a promising hydrogen source due to its high hydrogen content, abundant availability, nontoxic nature, and ease of storage and handling, making it particularly attractive for logistics-relevant and forward-operating energy platforms.[4–7] Among available reforming strategies, catalytic partial oxidation (CPOX) was selected due to its ability to enable rapid, on-demand operation within simplified system architectures. Its exothermic, self-sustaining nature eliminates the need for external heaters or steam supply, rendering it well-suited for compact, mobile, and field-deployable hydrogen generation systems.[8–11] While noble metals have demonstrated excellent catalytic performance in ethanol reforming, their high cost limits scalability, prompting the development of cost-effective alternatives using earth-abundant transition metals.[12,13]

Nickel (Ni)-based catalysts have been widely employed for ethanol reforming due to their cost-effectiveness, scalability, and high intrinsic activity toward C-C and C-H bond cleavage.[14–16] Under practical reforming conditions, however, Ni catalysts suffer from rapid deactivation caused by coke deposition and metal sintering, which limit long-term durability.[17] To mitigate these degradation pathways, CeO_2-based supports have been widely investigated as stabilization platforms for Ni-based reforming catalysts. Its intrinsic properties such as oxygen storage capacity and surface oxygen mobility enabled by the presence of Ce^{3+} and Ce^{4+} ions are critical in mitigating carbon deposition.[18–20] Moreover, structural modification of CeO_2 through aliovalent doping further improves these characteristics. The incorporation of gadolinium (Gd^{3+}) into the CeO_2 lattice introduces charge-compensating oxygen vacancies, resulting in the formation of Gd-doped CeO_2 (GDC). These vacancies significantly enhance surface oxygen mobility and lower the activation barrier for redox reactions, thereby promoting sustained surface regeneration and improved catalyst durability during ethanol reforming cycles.[21]

Beyond support engineering, incorporating small amounts of metals such as ruthenium (Ru) has been shown to improve water activation, hydrogen spillover, and catalyst regeneration, thereby enhancing the redox performance.[22,23] Previous studies have shown that Ru is highly effective in promoting reforming reactions involving various fuel precursors and improving fuel cell efficiency.[24–30] However, despite extensive studies on Ni-Ru catalysts and ceria-based materials, the coupled effects arising from Ru promotion and oxygen-vacancy-mediated redox behavior

in GDC-supported Ni catalysts in ethanol CPOX remain underexplored. While GDC provides abundant oxygen vacancies and high lattice oxygen mobility that support partial regeneration of active sites,[31–35] prior studies have not investigated how these vacancy-driven redox properties interact with Ru-facilitated, water-assisted redox pathways during ethanol CPOX. In particular, how this interaction influences sustained hydrogen production, suppression of carbonaceous by-products, and catalyst regeneration during long-term operations has yet to be clearly elucidated. A deeper understanding of these coupled mechanisms is essential for designing robust catalysts that can meet the practical requirements of distributed, field-deployable, and on-demand hydrogen generation systems.

In this study, we systematically investigate the promotional role of Ru and its synergistic interaction with Ni and GDC for ethanol CPOX by synthesizing catalysts with varying support (CeO_2 vs. GDC) and promoter compositions (Ni-only vs. Ni-Ru). To clarify the respective roles of oxygen vacancies in the support and Ru as a promoter, a series of catalysts were systematically designed by varying the support composition (CeO_2 vs. GDC) and metal configuration (Ni-only vs. Ni-Ru). This work aims to establish a clear structure-function framework for understanding how metal-support interactions and promoter effects influence catalytic behavior in ethanol CPOX, thereby providing design insights for advanced reforming catalysts.

2. Materials and Methods

2.1 Catalyst Preparation

Ni-CeO_2 (NC), Ni-GDC (NG), Ni/Ru-CeO_2 (NRC), and Ni/Ru-GDC (NRG) catalysts were synthesized via a wet impregnation method using $Ni(NO_3)_2 \cdot 6H_2O$ (Alfa Aesar), $RuCl_3 \cdot 3H_2O$ (Johnson Matthey), CeO_2 (Sigma-Aldrich), and GDC (20% Gd, Fuel Cell Materials) as precursors.[36–38] The total metal loading was fixed at 20 wt% for all catalysts. For monometallic systems (NC and NG), Ni accounted for the full metal fraction. For bimetallic catalysts (NRC and NRG), Ni and Ru were incorporated at a fixed weight ratio of 9:1. The remaining 80 wt% consisted of the oxide support (CeO_2 or GDC). These target loadings were calculated based on precursor molecular weights, and the impregnated mass ratio was maintained identically across all samples to enable direct comparison. The required amounts of metal salts were dissolved in a 1:1 mixture of ethanol and deionized water, followed by the addition of support powders into the solution. The mixture was stirred and heated at 60 °C until a gel-like consistency was achieved, then dried at 80 °C in a convection oven. The resulting solids were calcined at 450 °C for 3 h to obtain the catalyst powders. For the preparation of dip-coated catalysts, Al_2O_3 honeycomb

monoliths were immersed in a slurry composed of catalyst powder, deionized water, and polyvinylpyrrolidone in a 1:1 ratio using a dip coater (PTL-MM01). The coated monoliths were dried at 80 °C for 3 h and calcined at 450 °C for 3 h.

2.2 Characterization

X-ray diffraction (XRD) patterns were collected using a Bruker Phaser 2 diffractometer equipped with a Cu Kα radiation source. Catalyst morphology was examined using scanning electron microscopy (SEM; Phenom). Hydrogen temperature-programmed reduction (H_2-TPR) was performed using a chemisorption analyzer (AutoChem III 2930). 10 mg of catalyst was heated from room temperature to 900 °C at a rate of 10 °C/min under a flow of 10 vol% H_2 in He with a total flow rate of 50 sccm. X-ray photoelectron spectroscopy (XPS) analyses were conducted on reduced catalysts with a Phi 5000 VersaProbe III spectrometer. All spectra were calibrated to the adventitious C 1s peak at 284.8 eV. Peak deconvolution and fitting of the XPS spectra were performed using the PHI MultiPak software. Thermogravimetric analysis (TGA) was carried out using a TGA 7 instrument to evaluate coke accumulation by heating the samples to 800 °C at a rate of 10 °C/min in air.

2.3 Catalytic Testing

Catalytic activity tests were conducted in a continuous-flow fixed-bed quartz tubular reactor placed in a tube furnace and operated at 600 °C at a heating rate of 5 °C/min. For each test, 20 mg of catalyst was loaded into the reactor either in powder form or dip coated onto an Al_2O_3 honeycomb monolith. Prior to reaction, the catalysts were pre-reduced under 5% H_2/N_2 flow (100 sccm) at 600 °C for 40 min. After the reduction step, the reaction was directly initiated at 600 °C without intermediate cooling. Ethanol was supplied using a syringe pump at 0.02 mL/min, vaporized prior to mixing with air controlled by mass flow controller. Multiple O/C ratios (1.05–2.69) were initially screened by adjusting the air feed rate. Based on these preliminary evaluations, O/C = 1.6 was selected due to stable H_2 production and minimized formation of CH_4 and C_2 hydrocarbons. Under the final operating condition, air flow was fixed at 40 sccm and ethanol at 0.02 mL/min. Outlet gas flow was monitored using a mass flow meter to ensure total flow stability throughout the reaction. Reaction products were analyzed using a gas chromatograph (INFICON Micro GC), with calibration performed using certified gas standards (H_2, CO, CO_2, CH_4, C_2H_4, C_2H_6). After each experiment, the system was cooled under N_2 (100 sccm) at a controlled rate of 10 °C/min before sample removal. To ensure data reliability, each catalytic test was conducted until steady-state operation was achieved after an initial stabilization period. Product yields

were averaged over the steady-state region. Selected experiments were repeated under identical conditions to confirm reproducibility. Ethanol conversion (X_{EtOH}), H_2 yield (Y_{H_2}), and carbon-based product yields ($Y_{C,i}$) were calculated using the following equations[39–43]:

$$X_{EtOH} = \frac{F_{EtOH,in} - F_{EtOH,out}}{F_{EtOH,in}} \times 100$$

$$Y_{H_2} = \frac{F_{H_2}}{3 \cdot F_{EtOH,in}} \times 100$$

$$Y_{C,i} = \frac{F_i \cdot C_i}{2 \cdot F_{EtOH,converted}} \times 100$$

where $F_{EtOH,in}$ and $F_{EtOH,out}$ represent the inlet and outlet molar flow rates of ethanol, respectively; F_{H_2} represents the outlet molar flow rate of hydrogen; and F_i, C_i, and $F_{EtOH,converted}$ represent the molar flow rate of carbon-containing product i, number of carbon atoms in product i, and molar flow rate of ethanol consumed, respectively. For all catalytic tests, complete ethanol conversion (100%) was observed under the reaction conditions.

3. Results and Discussion

To evaluate the phase composition and crystallinity, XRD θ-2θ scans were conducted at room temperature for the NC, NRC, NG, and NRG catalysts. Figure 1a shows that all samples exhibited dominant diffraction patterns corresponding to fluorite-structured CeO_2 or GDC, indicating that the support phase remained largely preserved after catalyst synthesis (CeO_2: PDF #81-0792). Additional reflections observed at approximately 37.2°, 43.2°, 62.9°, and 75.5° were assigned to NiO (PDF #78-0643), confirming the presence of NiO species across all samples. Due to the relatively low loading of Ru (total metal loading = 20 wt%, Ni/Ru = 9:1), no distinct Ru-related reflections were detected in the NRC and NRG samples. XRD patterns collected after H_2 reduction (Figure 1b) showed the disappearance of NiO reflections and the emergence of metallic Ni peaks (PDF #89-7128), confirming the effective reduction of nickel oxide during catalyst activation. The fluorite structure of CeO_2 and GDC remained unchanged after reduction, confirming the structural stability of the supports under reductive conditions.

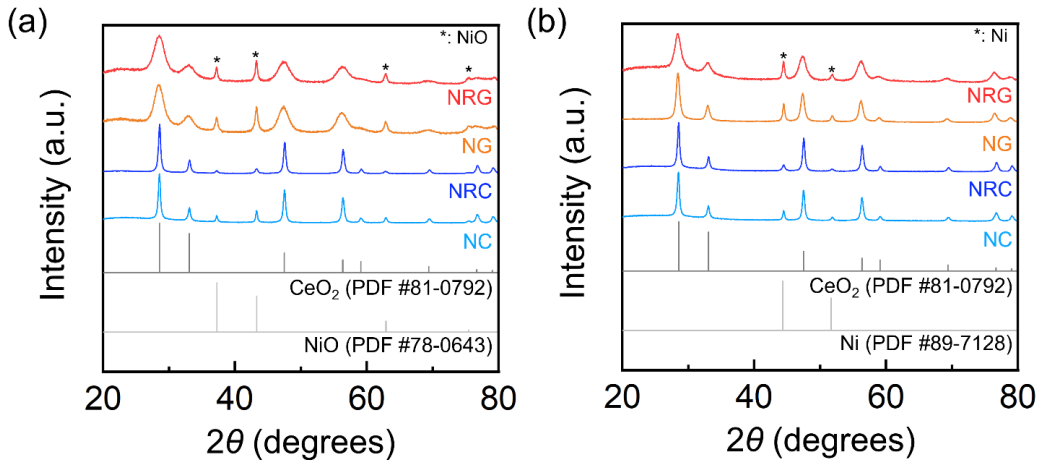

Figure 1. XRD patterns of (a) as-synthesized and (b) reduced NC, NRC, NG, and NRG.

The morphology of the NRC and NRG catalysts after reduction was examined using SEM (Figure 2a,b). Both catalysts exhibited surfaces decorated with uniformly distributed Ni nanoparticles. Energy dispersive spectroscopy (EDS) elemental mapping of the NRG catalyst (Figure 2c) confirmed that Ni nanoparticles (red) were well dispersed on the GDC support (green). Ru is not shown in this mapping due to its relatively low loading. Nevertheless, its presence within the catalyst structure was verified through the corresponding EDS spectrum (Figure 3), confirming the successful incorporation of both active metals onto the GDC support.

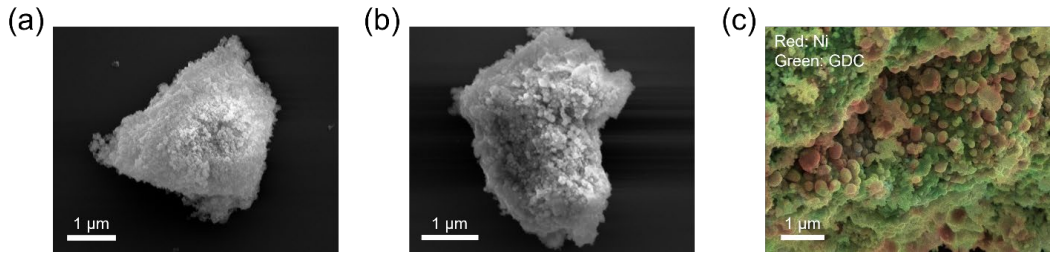

Figure 2. SEM images of (a) NRC and (b) NRG catalysts, and (c) EDS elemental mapping of NRG, where red denotes Ni and green denotes the GDC support. Ru is not visible in the mapping due to its low loading, but its presence was confirmed by EDS spectrum in Figure 3.

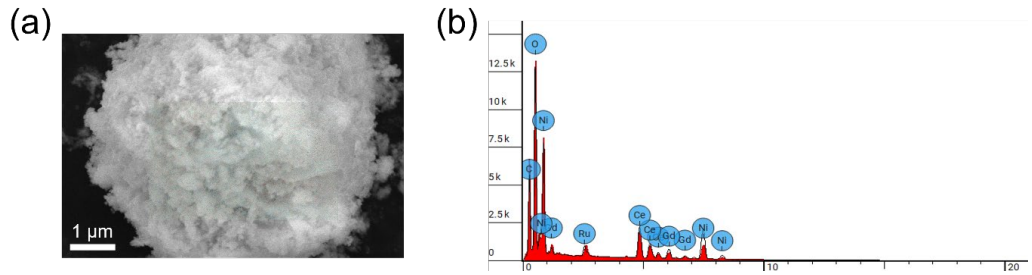

Figure 3. (a) SEM image of the NRG catalyst and (b) corresponding EDS spectrum.

Average yields of H_2, CO, CO_2, CH_4, C_2H_4, and C_2H_6 were measured by GC after ethanol CPOX reactions conducted at 600 °C using an O/C ratio of 1.6 over NC, NRC, NG, and NRG catalysts. The O/C ratio of 1.6 was selected because it produced relatively high yields of H_2 and CO while minimizing the formation of CH_4 and C_2 hydrocarbons (Figure 4), thereby providing a stable operating window that balanced oxidation and reforming with suppressed side reactions. It is important to note that Ru was carefully selected as a promoter due to its unique ability to facilitate water activation, enhance surface oxygen mobility, and accelerate redox cycling.[22,23,44,45]

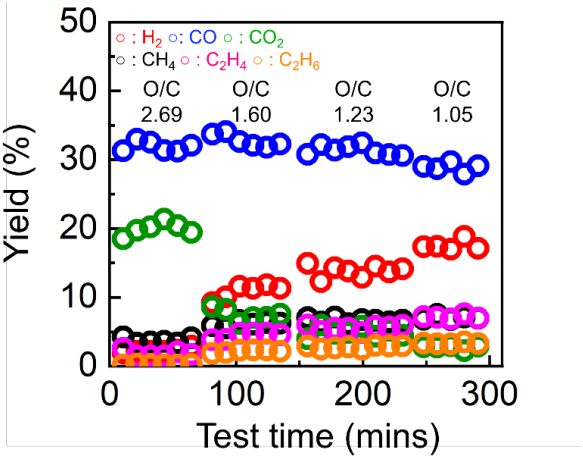

Figure 4. Product yield profiles obtained from blank ethanol CPOX tests conducted at 600 °C under different O/C ratios.

Figure 5a shows that alternative secondary metals (Cu, Fe, Co, Mo) added to NG did not yield significant improvements. Optimization of the Ni:Ru ratio further showed that while a 9.5:0.5 composition improved performance relative to NG, it was less effective than the 9:1 ratio. Increasing the Ru content beyond this point provided no additional benefit, thereby establishing the Ni/Ru ratio of 9:1 as the optimal balance for catalytic performance (Figure 5b).

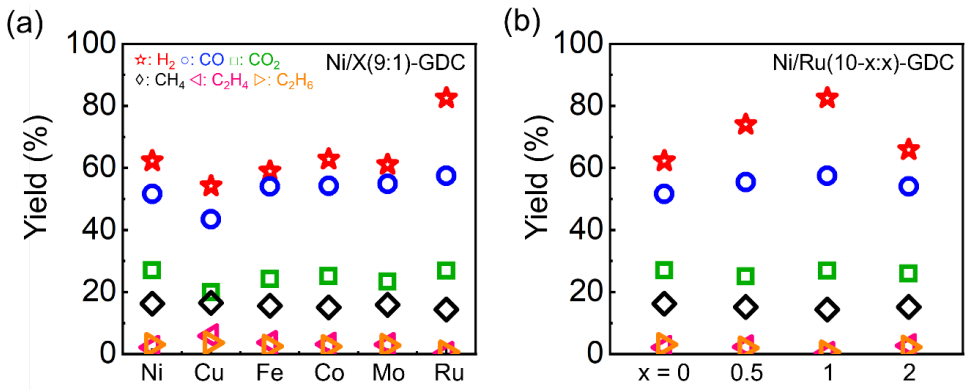

Figure 5. Product yields during ethanol CPOX at 600 °C over Ni-based catalysts supported on GDC. (a) Average yields of H_2, CO, CO_2, CH_4, C_2H_4, and C_2H_6 over Ni/X(9:1)-GDC catalysts with various secondary metals (X = Cu, Fe, Co, Mo, Ru). (b) Yields over Ni/Ru(10-x:x)-GDC catalysts with varying Ru content (x = 0, 0.5, 1, 2). Each data point represents the average over a 5-h test.

Figure 6a shows that NG exhibited a notable increase in H_2 yield compared with NC, indicating the beneficial effect of the GDC support. Incorporation of Ru into NG (NRG) significantly enhanced H_2 production and reduced CH_4 and C_2 hydrocarbon formation (Figure 6b), whereas the same Ru addition to NC (NRC) resulted in minimal change. Although differences in support crystallite size or surface area could influence the density of accessible sites, the distinct performance trends observed here, particularly the asymmetric response to Ru promotion between CeO_2- and GDC-supported catalysts, indicated that enhanced CPOX performance could not be attributed to size-related effects alone. Instead, the observed performance trends were consistent with cooperative interactions among Ni active sites, Ru promoter, and the oxygen-vacancy-rich GDC support. The GDC support supplied mobile lattice oxygen that participated in the oxidation of carbon species, thereby mitigating coke accumulation on the Ni surface.[46] Concurrently, Ru promoted surface redox processes and facilitated the regeneration of oxygen-deficient sites in the oxygen-vacancy-rich GDC support. This cooperative mechanism enabled a continuous cycle in which GDC oxidized surface carbon species and Ru assisted in regenerating the oxygen-deficient sites, thereby sustaining catalyst activity during ethanol reforming.[29,47,48] This interpretation was supported by TGA analysis of catalysts recovered after short-term CPOX operation (~5 h), where the NRG catalyst exhibited significantly lower weight loss, indicating suppressed coke formation during the initial reaction period (Figure 7). In this oxidative environment, enhanced oxygen mobility and rapid replenishment of surface oxygen promoted higher H_2 and CO formation and suppressed non-oxidative pathways that lead to CH_4 and C_2 hydrocarbons.[49,50] This suppression was attributed to the inhibition of ethanol pyrolysis and cracking routes, thereby favoring selective partial oxidation via redox-assisted mechanisms.[51]

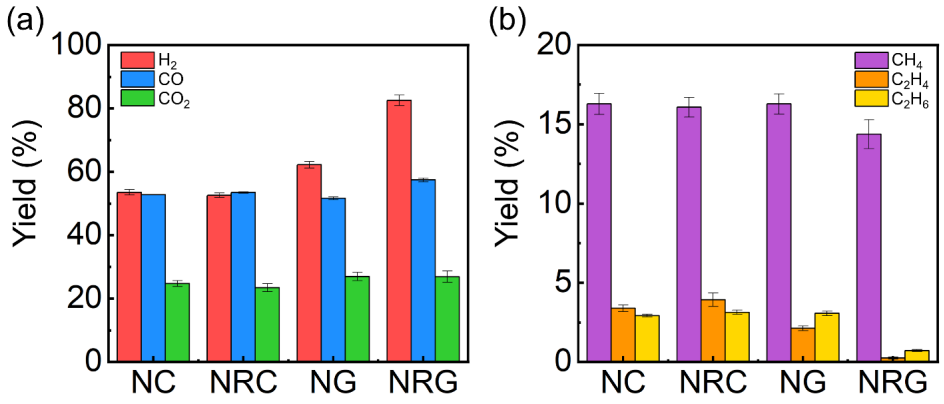

Figure 6. Average yields of (a) H_2, CO, and CO_2, and (b) CH_4, C_2H_4, and C_2H_6 during ethanol CPOX at 600 °C over 5 h for catalysts NC, NRC, NG, and NRG. Reactions were conducted in a fixed-bed quartz reactor using 20 mg of catalyst with an O/C ratio of 1.6.

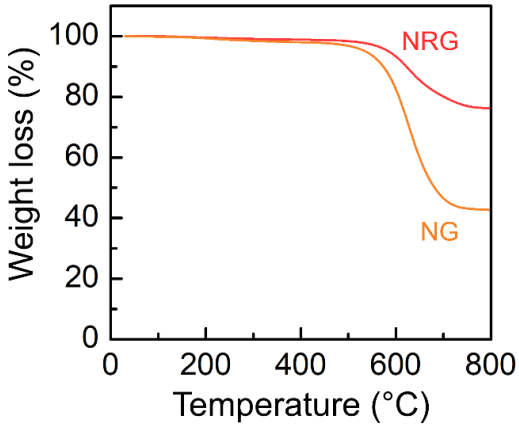

Figure 7. TGA of NG and NRG catalysts after 5-h ethanol CPOX testing at 600 °C.

To further assess the promotional role of Ru and its cooperative interaction with Ni and GDC support, H_2-TPR measurements were performed for CeO_2 and GDC supports, as well as NC, NG, NRC, and NRG catalysts, as summarized in Figure 8. The profiles of the bare supports showed that GDC exhibited a lower overall reduction temperature compared with CeO_2, which was consistent with the presence of oxygen vacancies introduced by Gd doping. In general, H_2-TPR profiles of CeO_2-based materials show two distinct regions: a low-temperature peak (300–600 °C), corresponding to the reduction of surface Ce^{4+} to Ce^{3+}, and a higher-temperature peak (700–800 °C), attributed to the bulk lattice reduction.[52–58] For GDC, the reduction peaks were shifted to lower temperatures relative to CeO_2, indicating enhanced reducibility. This shift was attributed to the higher concentration of oxygen vacancies, which facilitated lattice oxygen mobility on the GDC surface and lowered the activation barrier for reduction.[52,59] Notably, the main NiO reduction peak of NG (~365 °C) occurred at a slightly higher temperature than that of NC (~335 °C), despite the higher intrinsic reducibility of GDC. This

behavior was consistent with stronger metal-support interactions in the NG system, where increased oxygen vacancy concentration likely led to stronger anchoring of Ni species, thereby requiring higher temperatures for reduction.[60] Upon incorporation of Ru into NG to form the NRG catalyst, the NiO reduction peak shifted substantially to approximately 310 °C, along with two additional low-temperature reduction peaks at approximately 120 °C and 155 °C, which were assigned to the sequential reduction of RuO_2 species.[61,62] Compared with the corresponding NiO reduction peak in NG (~365 °C) and RuO_2-related reduction peak observed for NRC (~189 °C), NRG catalyst exhibited significant peak shifts to lower temperatures, suggesting that active hydrogen species adsorbed on pre-reduced Ru sites could spill over to adjacent NiO, thereby facilitating its reduction on the GDC surface.[63–65] These shifts also reflected enhanced surface reducibility in NRG, likely associated with the high oxygen vacancy density of the GDC support, which promoted adsorption of more readily reducible oxygen species and increased H_2 consumption at low temperatures.[54,66] Collectively, the H_2-TPR results were consistent with cooperative interactions among Ni, Ru, and the oxygen-vacancy-rich GDC support, contributing to the enhanced redox behavior in the NRG catalyst system.

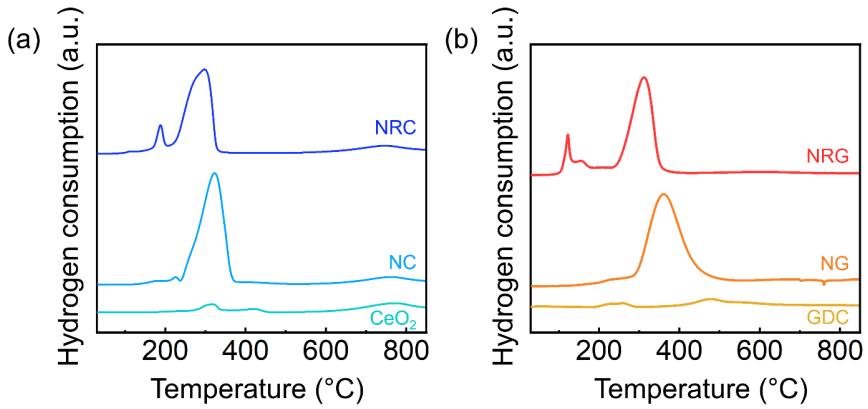

Figure 8. H_2-TPR profiles of (a) CeO_2, NC, and NRC, and (b) GDC, NG, and NRG catalysts.

The surface electronic structures of reduced NRC and NRG catalysts were investigated by XPS, as summarized in Figure 9 and Table 1. Analysis of the Ni 2p region (Figure 9a) was performed to assess metal reducibility, since the Ru peak overlapped with the intense C 1s signal (~285 eV) and the Ru loading was relatively low (Ni:Ru = 9:1 within ~20 wt% total metal). The spectra revealed the coexistence of both oxidized (Ni^{2+}) and metallic (Ni^0) states, with NRG (32%) exhibiting a larger fraction of metallic Ni than NRC (8.9%), consistent with the enhanced surface reducibility observed in the H_2-TPR profiles. Notably, the Ni 2p peaks of NRG were shifted to slightly higher binding energies compared with those of NRC,

which was consistent with stronger metal-support interactions between Ni species and the oxygen-vacancy-rich GDC support.[67–69] The O 1s spectra (Figure 9b) were deconvoluted into four oxygen species: chemisorbed water (O_W), surface-adsorbed defect-related oxygen species (O_S), hydroxyl groups (O_{OH}), and lattice oxygen (O_L). Compared with NRC (1.8%), the NRG catalyst (10.5%) exhibited a higher concentration of O_W, indicating increased availability of water-related surface species associated with the combined presence of Ni, Ru, and the oxygen-vacancy-rich GDC support, which was favorable for suppressing coke deposition.[29] In addition, the O 1s features of NRG showed a systematic shift toward higher binding energies, following the same trend observed for the Ni 2p spectra. This concurrent shift suggested a modified surface oxygen environment consistent with a more defect-rich, vacancy-prone oxide support.[70] In line with these observations, the Ce 3d spectra (Figure 9c) showed a higher Ce^{3+} fraction for NRG compared with NRC. Taken together, the combined XPS and H_2-TPR results were consistent with higher surface reducibility, increased defect-related surface characteristics, and enhanced availability of water-related surface species in the NRG catalyst, correlating with its improved catalytic performance and resistance to coke formation.

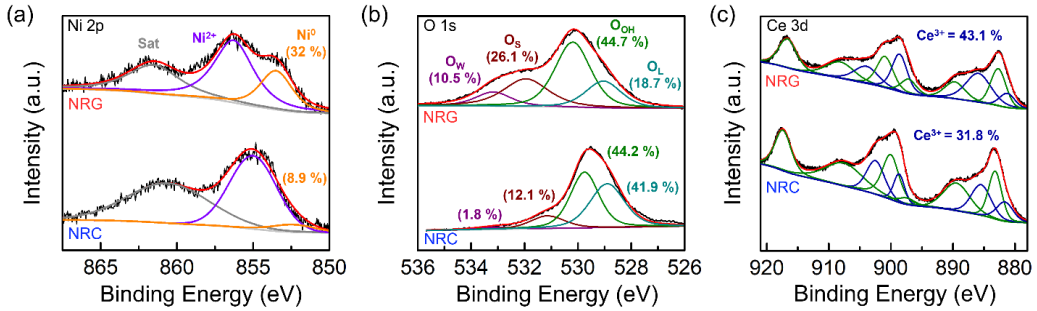

Figure 9. XPS of (a) Ni 2p, (b) O 1s, and (c) Ce 3d for reduced NRC and NRG catalysts. Elemental concentrations are presented in mol%.

Table 1. Binding energy (eV) of Ni, O, and Ce.

Sample	Ni 2p, eV		
	Ni^0	Ni^{2+}	Sat
NRG	853.49	856.27	861.52
NRC	852.37	855.01	860.6

Sample	O 1s, eV			
	O_L	O_{OH}	O_S	O_W
NRG	529.04	530.19	531.95	533.17
NRC	528.9	529.75	531.14	533.02

Sample	Ce 3d 5/2, eV					Ce 3d 3/2, eV				
	Ce^{3+}		Ce^{4+}			Ce^{3+}		Ce^{4+}		
NRG	881.24	885.88	882.68	889.68	897.13	898.6	903.95	900.96	908.14	916.66
NRC	881.62	885.45	883.20	889.42	897.46	898.67	902.46	900.03	907.55	917.39

To further evaluate the role of Ru in enhancing water-involving pathways and redox performance, the H_2/CO ratio and CH_4 selectivity were evaluated, as summarized in Figure 10. In ethanol CPOX, water can participate through pathways such as CO + H_2O → CO_2 + H_2 and CH_4 + H_2O → CO + 3H_2.[71,72] The NRG catalyst, which incorporated Ru into NG, exhibited an increased H_2/CO ratio, indicating enhanced involvement of water-assisted reactions during ethanol conversion (Figure 10a). In contrast, the addition of Ru to NC (NRC) resulted in a slight decrease in the H_2/CO ratio. This difference was attributed to the lower oxygen vacancy density of the CeO_2 support, which limited redox cycling and the effective involvement of water-derived species in CO conversion and associated H_2 formation.[73,74] In addition, the CH_4 selectivity of NRG was significantly lower than that of NC, NRC, and NG, indicating suppressed methane formation (Figure 10b). This suppression was favorable, as CH_4 is typically produced via non-oxidative pathways such as ethanol hydrogenation or decomposition, which compete with partial oxidation and reduce hydrogen yield. The persistence of relatively high CH_4 selectivity in NG, despite its oxygen-vacancy-rich GDC support, suggested that GDC alone was not sufficient to fully suppress these undesired pathways. By contrast, incorporation of Ru into NG (NRG) modified the surface reaction environment by enhancing water-assisted redox processes, which facilitated the oxidation of carbonaceous intermediates prior to their conversion to methane.[75,76] Overall, the reduced CH_4 selectivity and increased H_2/CO ratio observed for NRG were consistent with enhanced oxidative reaction pathways enabled by the combined presence of Ru and the oxygen-vacancy-rich GDC support, resulting in improved hydrogen yield and reduced formation of undesirable by-products.

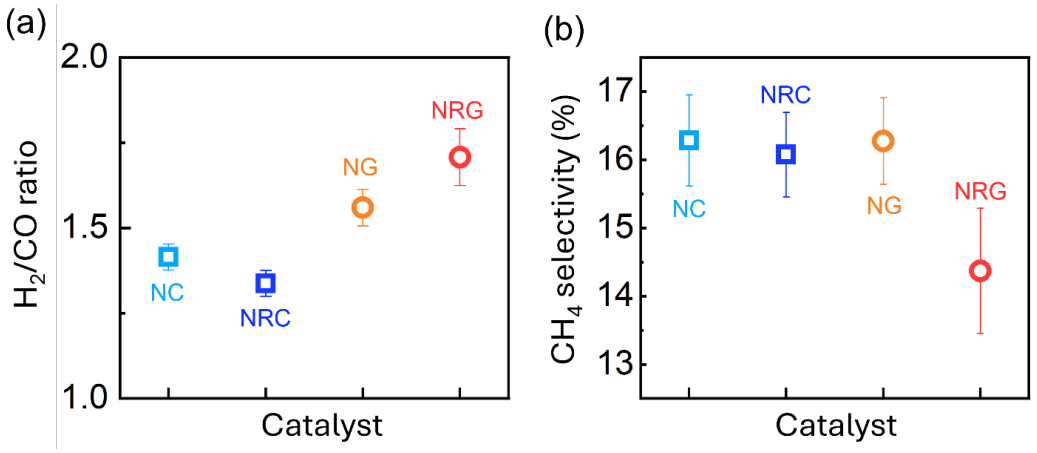

Figure 10. H_2/CO ratio and CH_4 selectivity of NC, NRC, NG, and NRG catalysts during ethanol CPOX at 600 °C.

To evaluate the practical applicability of the NC, NG, NRC, and NRG catalysts, a long-term stability test was performed, as summarized in Figure 11. For this test, the catalysts were dip-coated onto a commercially available Al_2O_3 honeycomb monolith, which offered mechanical robustness, high geometric surface area, and efficient gas-solid contact, thereby making it suitable for real-world catalytic applications.[77–79] The NG catalyst exhibited a slower deactivation rate (–0.67 %/h) compared with NC (–1.32 %/h), showing the stabilizing role of GDC's higher oxygen vacancy density and superior lattice oxygen mobility. In contrast, CeO_2, with its lower vacancy density, was more susceptible to oxygen depletion under prolonged operation, reducing its ability to oxidize carbon deposits. Incorporation of a small amount of Ru into both NG and NC moderated the deactivation rate. While Ru reduced the stability gap between GDC- and CeO_2-supported catalysts, NRG consistently maintained an approximately 10% higher H_2 yield than NRC throughout the test, consistent with the combined effect of Ru incorporation and the oxygen-vacancy-rich GDC support. Notably, both NRC and NRG displayed slope changes in their deactivation profiles after approximately 1,200–1,500 min.

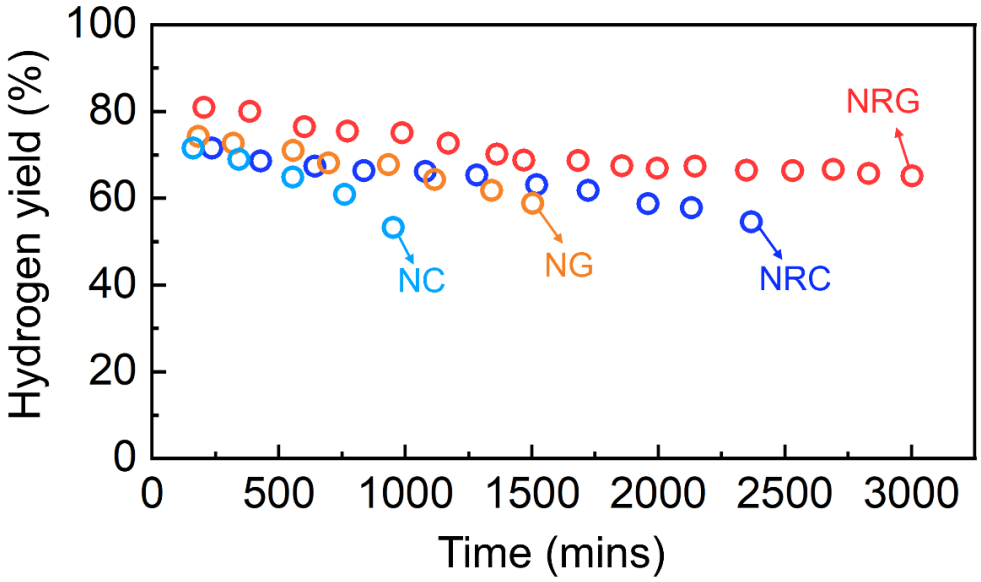

Figure 11. Long-term hydrogen yield stability of NC, NG, NRC, and NRG catalysts coated on an Al_2O_3 honeycomb monolith during ethanol CPOX at 600 °C with an O/C ratio of 1.6.

For NRC, the slope shifted from –0.49 to –0.59 %/h, suggesting a transition from kinetically controlled operation to a diffusion-limited regime, where carbon accumulation progressively restricted steam and oxygen access to the catalyst surface, thereby suppressing H_2-forming reactions.[42,80,81] In contrast, NRG transitioned from –0.54 to a gradual decay of –0.15 %/h, sustaining approximately 80% of its initial hydrogen yield for approximately 50 h. This stabilized regime was consistent with a redox-assisted regenerative mechanism involving cooperative

interactions among Ni, Ru, and the GDC support, where lattice oxygen from GDC oxidized carbon deposits, Ru facilitated hydrogen spillover and sustained surface redox cycling, and Ni continued to cleave C-C and C-H bonds, collectively slowing H_2 yield loss under diffusion-limited conditions. This interpretation was supported by TGA of catalysts collected after the long-term tests, where NRG exhibited substantially lower weight loss than NRC, indicating reduced coke accumulation (Figure 12). Consistently, SEM images of spent catalysts revealed extensive carbon fiber formation on NRC, whereas the NRG catalyst remained largely free of filamentous carbon deposits (Figure 13). These observations collectively confirmed that the NRG catalyst sustained high hydrogen yield and long-term stability in ethanol CPOX, where its strong coke resistance ensured an extended lifetime and highlighted its potential for practical reforming applications.

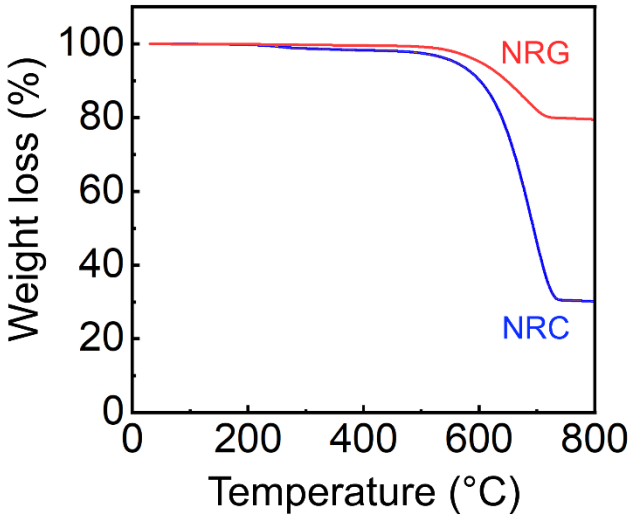

Figure 12. TGA of NRC and NRG catalysts after long-term ethanol CPOX testing at 600 °C.

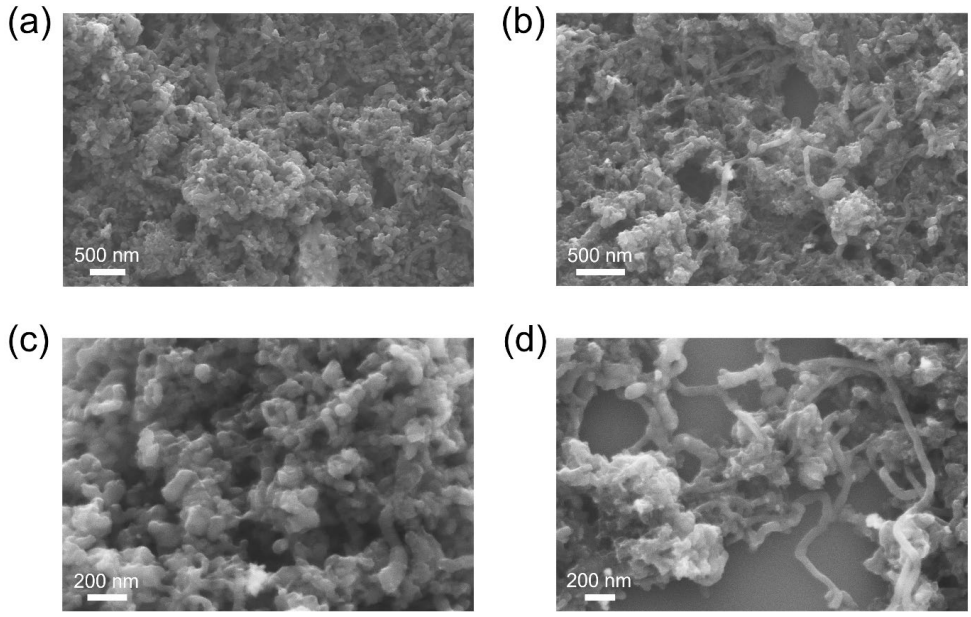

Figure 13. SEM images of (a) NRG and (b) NRC catalysts after long-term ethanol CPOX operation, and corresponding higher-magnification images of (c) NRG and (d) NRC, highlighting differences in carbon deposition morphology.

4. Conclusion

In this work, we examined the synergistic effects of Ni, Ru, and oxygen-vacancy-rich GDC in ethanol CPOX. Compared with NC, the NG catalyst exhibited higher hydrogen yield, indicating that oxygen vacancies enhanced surface oxygen mobility and facilitated catalyst self-regeneration. Additional promotion with Ru to form the NRG catalyst led to further improvements, including increased hydrogen production, suppressed hydrocarbon by-products, and extended catalyst lifetime. Gas analysis of the NRG catalyst revealed the highest H_2/CO ratio and the lowest CH_4 selectivity among all catalysts, consistent with enhanced participation of water-involving pathways and effective suppression of undesired reaction routes. XPS and H_2-TPR results showed that both Gd doping and Ru incorporation enhanced reducibility, increased defect-related surface characteristics, and improved the availability of water-related surface species. In particular, Ru in the NRG catalyst facilitated NiO reduction through hydrogen spillover, while the oxygen-vacancy-rich GDC support promoted sustained redox cycling. Long-term stability testing, together with post-reaction TGA and SEM analyses, confirmed reduced coke accumulation on the NRG catalyst, supporting a redox-assisted regenerative mechanism enabled by the combined presence of Ru and GDC. These results highlighted the critical role of oxygen vacancies and metal-support interactions in achieving durable, coke-resistant catalytic performance. Overall, this study provided mechanistic insights and practical design guidance for the development of robust CPOX catalysts suitable for distributed hydrogen generation applications.

5. References

1. Dou B, Song Y, Wang C, Chen H, Xu Y. Hydrogen production from catalytic steam reforming of biodiesel byproduct glycerol: issues and challenges. Renew Sustain Energy Rev. 2014;30:950–960.

2. Mattos LV, Jacobs G, Davis BH, Noronha FB. Production of hydrogen from ethanol: review of reaction mechanism and catalyst deactivation. Chem Rev. 2012;112:4094–4123.

3. Iulianelli A, Ribeirinha P, Mendes A, Basile A. Methanol steam reforming for hydrogen generation via conventional and membrane reactors: a review. Renew Sustain Energy Rev. 2014;29:355–368.

4. Chaubey R, Sahu S, James OO, Maity S. A review on development of industrial processes and emerging techniques for production of hydrogen from renewable and sustainable sources. Renew Sustain Energy Rev. 2013;23:443–462.

5. Zanchet D, Santos JBO, Damyanova S, Gallo JMR, Bueno JMC. Toward understanding metal-catalyzed ethanol reforming. ACS Catal. 2015;5:3841–3863.

6. Ni M, Leung DY, Leung MK. A review on reforming bio-ethanol for hydrogen production. Int J Hydrog Energy. 2007;32:3238–3247.

7. Augusto BL, Costa LO, Noronha FB, Colman RC, Mattos LV. Ethanol reforming over Ni/CeGd catalysts with low Ni content. Int J Hydrog Energy. 2012;37:12258–12270.

8. Ma R, Xu B, Zhang X. Catalytic partial oxidation (CPOX) of natural gas and renewable hydrocarbons/oxygenated hydrocarbons - a review. Catal Today 2019;338:18–30.

9. Hohn KL, Lin YC. Catalytic partial oxidation of methanol and ethanol for hydrogen generation. ChemSusChem. 2009;2:927–940.

10. Jung H et al. Fast start-up reactor for partial oxidation of methane with electrically-heated metallic monolith catalyst. J Power Sources. 2003;124: 76–80.

11. Chen WH et al. A critical and systematic review of sustainable hydrogen production from ethanol/bioethanol: steam reforming, partial oxidation, and autothermal reforming. Fuel. 2023;333:126526.

12. Rosha P, Ali FM, Ibrahim H. Recent advances in hydrogen production through catalytic steam reforming of ethanol: advances in catalytic design. Can J Chem Eng. 2023;101:5498–5518.

13. Ogo S, Sekine Y. Recent progress in ethanol steam reforming using non-noble transition metal catalysts: a review. Fuel Process Technol. 2020;199:106238.

14. Xu W et al. Steam reforming of ethanol on Ni/CeO_2: reaction pathway and interaction between Ni and the CeO_2 support. ACS Catal. 2013;3:975–984.

15. Liu Z et al. Ambient pressure XPS and IRRAS investigation of ethanol steam reforming on Ni-CeO_2(111) catalysts: an in situ study of C-C and O-H bond scission. Phys Chem Chem Phys. 2016;18:16621–16628.

16. Fatsikostas AN, Verykios XE. Reaction network of steam reforming of ethanol over Ni-based catalysts. J Catal. 2004;225:439–552.

17. Karim AM et al. A comparative study between Co and Rh for steam reforming of ethanol. Appl Catal B. 2010;96:441–448.

18. Gupta A, Waghmare U, Hegde M. Correlation of oxygen storage capacity and structural distortion in transition-metal-, noble-metal-, and rare-earth-ion-substituted CeO_2 from first principles calculation. Chem Mater. 2010;22:5184–5198.

19. Kehoe AB, Scanlon DO, Watson GW. Role of lattice distortions in the oxygen storage capacity of divalently doped CeO_2. Chem Mater. 2011;23:4464–4468.

20. Silva AGM et al. $Ce_{1-x}Sm_xO_{1.9-\delta}$ nanoparticles obtained by microwave-assisted hydrothermal processing: an efficient application for catalytic oxidation of α-bisabolol. Catal Sci Technol. 2014;4:814–821.

21. Tojira O, Lomonaco JG, Sesuk T, Charojrochkul S, Tepamatr P. Enhancement of hydrogen production using Ni catalysts supported by Gd-doped ceria. Heliyon. 2021;7:e08202.

22. Koh ACW et al. Ethanol steam reforming over supported ruthenium and ruthenium-platinum catalysts: comparison of organometallic clusters and inorganic salts as catalyst precursors. Int J Hydrog Energy. 2009;34:5691–5703.

23. Utaka T, Okanishi T, Takeguchi T, Kikuchi R, Eguchi K. Water gas shift reaction of reformed fuel over supported Ru catalysts. Appl Catal A. 2003;245:343–351.

24. Quach Trinh Hong D, Do BL, Ha CA, Nguyen T, Cam Loc L. Role of ruthenium in modified $CeNi_{1-x}Ru_xO_3$ perovskite catalysts for the bireforming of methane. Energy Fuels. 2025;39:1341–1361.

25. Carbajal-Ramos IA et al. Catalytic behavior of Ru supported on $Ce_{0.8}Zr_{0.2}O_2$ for hydrogen production. Appl Catal B. 2016;181:58–70.

26. Hung CC, Chen SL, Liao YK, Chen CH, Wang JH. Oxidative steam reforming of ethanol for hydrogen production on M/Al_2O_3. Int J Hydrog Energy. 2012;37:4955–4966.

27. Liguras DK, Kondarides DI, Verykios XE. Production of hydrogen for fuel cells by steam reforming of ethanol over supported noble metal catalysts. Appl Catal B. 2003;43:345–354.

28. Chiu WC, Horng RF, Chou HM. Hydrogen production from an ethanol reformer with energy saving approaches over various catalysts. Int J Hydrog Energy. 2013;38:2760–2769.

29. Liu F et al. Synergistic effects of in-situ exsolved Ni-Ru bimetallic catalyst on high-performance and durable direct-methane solid oxide fuel cells. J Am Chem Soc. 2024;146:4704–4715.

30. Liu F et al. Process-intensified protonic ceramic fuel cells for power generation, chemical production, and greenhouse gas mitigation. Joule. 2023;7:1308–1332.

31. Yang G et al. Tuning ionic conductivity in fluorite Gd-doped CeO_2-bixbyite RE_2O_3 (RE = Y and Sm) multilayer thin films by controlling interfacial strain. ACS Appl Electron Mater. 2023;5:4556–4563.

32. Park HJ, Choi GM. Oxygen permeability of gadolinium-doped ceria at high temperature. J Eur Ceram Soc. 2004;24:1313–1317.

33. Sadykov VA et al. Mobility and reactivity of lattice oxygen in Gd-doped ceria promoted by Pt. React Kinet Catal Lett. 2005;85:367–373.

34. Xiao Y, Li H, Xie K. Activating lattice oxygen at the twisted surface in a mesoporous CeO_2 single crystal for efficient and durable catalytic CO oxidation. Angew Chem Int Ed. 2021;60:5240–5244.

35. Lin G, Li H, Xie K. Identifying and engineering active sites at the surface of porous single-crystalline oxide monoliths to enhance catalytic activity and stability. CCS Chem. 2022;4:1441–1451.

36. Sietsma JRA et al. Ordered mesoporous silica to study the preparation of Ni/SiO_2 ex nitrate catalysts: impregnation, drying, and thermal treatments. Chem Mater. 2008;20:2921–2931.

37. Hassani Rad SJ, Haghighi M, Alizadeh Eslami A, Rahmani F, Rahemi N. Sol-gel vs. impregnation preparation of MgO and CeO_2 doped Ni/Al_2O_3 nanocatalysts used in dry reforming of methane: effect of process conditions, synthesis method and support composition. Int J Hydrog Energy. 2016;41:5335–5350.

38. Chouillet C, Villain F, Kermarec M, Lauron-Pernot H, Louis C. Relevance of the drying step in the preparation by impregnation of Zn/SiO_2 supported catalysts. J Phys Chem B. 2003;107:3565–3575.

39. Ferreira GR, Nogueira FGE, Lucrédio AF, Assaf EM. Ethanol steam reforming by Ni catalysts for H_2 production: evaluation of Gd effect in CeO_2 support. Catal Lett. 2022;152:3125–3145.

40. Sawatmongkhon B et al. Hydrogen production via the catalytic partial oxidation of ethanol on a platinum–rhodium catalyst: effect of the oxygen-to-ethanol molar ratio and the addition of steam. Energy Fuels. 2019;33:6742–6753.

41. Iulianelli A, Liguori S, Calabrò V, Pinacci P, Basile A. Partial oxidation of ethanol in a membrane reactor for high purity hydrogen production. Int J Hydrog Energy. 2010;35:12626–12634.

42. Iglesias-Vázquez S et al. Global vision of the reaction and deactivation routes in the ethanol steam reforming on a catalyst derived from a Ni-Al spinel. Energy Fuels. 2024;38:7033–7048.

43. Ruocco C, Palma V, Ricca A. Hydrogen production by oxidative reforming of ethanol in a fluidized bed reactor using a $PtNi/CeO_2SiO_2$ catalyst. Int J Hydrog Energy. 2019;44:12661–12670.

44. Chronister CW, Binstead RA, Ni J, Meyer TJ. Mechanism of water oxidation catalyzed by the μ-oxo dimer $(bpy)_2(OH_2)RuIIIORuIII(OH_2)(bpy)_2]^{4+}$. Inorg Chem. 1997;36:3814–3815.

45. Jurss JW, Concepcion JC, Norris MR, Templeton JL, Meyer TJ. Surface catalysis of water oxidation by the blue ruthenium dimer. Inorg Chem. 2010;49:3980–3982.

46. Yang Z, Fu Z, Zhang Y, Wu R. Direct CO oxidation by lattice oxygen on Zr-doped ceria surfaces. Catal Lett. 2011;141:78–82.

47. Vecchietti J et al. Understanding the role of oxygen vacancies in the water-gas shift reaction on ceria-supported platinum catalysts. ACS Catal. 2014;4:2088–2096.

48. Mathew S et al. Enhanced electrocatalytic water splitting by Sm- and Gd-doped ceria electrocatalysts on Ni foam substrate. Electrochim Acta. 2022;435:141382.

49. Zhang C et al. Enhanced oxygen mobility and reactivity for ethanol steam reforming. AIChE J. 2012;58:516–525.

50. Crowley S, Castaldi MJ. Mechanistic insights into catalytic ethanol steam reforming using isotope-labeled reactants. Angew Chem Int Ed. 2016;55:10650–10655.

51. Dancini-Pontes I, Fernandes-Machado NRC, de Souza M, Pontes RM. Insights into ethanol decomposition over Pt: a DFT energy decomposition analysis for the reaction mechanism leading to C_2H_6 and CH_4. Appl Catal A. 2015;491:86–93.

52. Kim M, Park G, Jo K, Lee H. Enhanced redox properties of Gd-doped CeO_2-TiO_2 induced by oxygen vacancies and disordered structure. Mater Today Chem. 2023;29:101440.

53. Marrero-Jerez J, Larrondo S, Rodríguez-Castellón E, Núñez P. TPR, XRD and XPS characterisation of ceria-based materials synthesized by freeze-drying precursor method. Ceram Int. 2014;40:6807–6813.

54. Zhang B, Zhang S, Liu B. Effect of oxygen vacancies on ceria catalyst for selective catalytic reduction of NO with NH_3. Appl Surf Sci. 2020;529:147068.

55. Sohn H et al. Oxygen mobility in pre-reduced nano- and macro-ceria with Co loading: an AP-XPS, in-situ DRIFTS and TPR study. Catal Lett. 2017;147:2863–2876.

56. Chen D et al. Investigation of the role of surface lattice oxygen and bulk lattice oxygen migration of cerium-based oxygen carriers: XPS and designed H_2-TPR characterization. Appl Catal B Environ Energy. 2017;218:249–259.

57. Hojo H, Hirota K, Ito S, Einaga H. Reduction mechanism for CeO_2 revealed by direct observation of the oxygen vacancy distribution in shape-controlled CeO_2. Adv Mater Interf. 2023;10:2201954.

58. Liu P, Niu R, Li W, Wang S, Li J. Morphology effect of ceria on the ammonia synthesis activity of Ru/CeO_2 catalysts. Catal Lett. 2019;149:1007–1016.

59. Chanapattharapol KC, Krachuamram S, Kidkhunthod P, Poo-arporn Y. The effect of Sm addition on structure, redox properties and catalytic activities for water-gas shift reaction of ceria-based support. Solid State Sci. 2020;99:106066.

60. Xiao Z et al. Engineering oxygen vacancies and nickel dispersion on CeO_2 by Pr doping for highly stable ethanol steam reforming. Appl Catal B. 2019;258:117940.

61. Trovarelli A. Catalytic properties of ceria and CeO_2-containing materials. Catal Rev. 1996;38:439–520.

62. Wang L, Chen J, Patel A, Rudolph V, Zhu Z. Catalytic performance of Ru nanoparticles supported on different mesoporous silicas for preferential oxidation of CO in H_2-rich atmosphere. Appl Catal A. 2012;447:200–209.

63. Yao N et al. Effect of cation-oligomer interactions on the size and reducibility of NiO particles on NiRu/SiO_2 catalysts. J Mater Chem. 2011;21:17403–17412.

64. Park JH, Chang TS. Promotional effect of ruthenium addition to Co/α-Al_2O_3 catalyst for dry reforming of methane. Catal Lett. 2019;149:3148–159.

65. Shun K et al. Revealing hydrogen spillover pathways in reducible metal oxides. Chem Sci. 2022;13:8137–8147.

66. Sakpal T, Lefferts L. Structure-dependent activity of CeO_2 supported Ru catalysts for CO_2 methanation. J Catal. 2018;367:171–182.

67. Fung SC. XPS studies of strong metal-support interactions (SMSI)—PtTiO_2. J Catal. 1982;76:225–230.

68. Ho PH et al. Ru–CeO_2 and Ni–CeO_2 coated on open-cell metallic foams by electrodeposition for the CO_2 methanation. Ind Eng Chem Res. 2021;60:6730–6741.

69. Khatun R et al. Ni/$Ce_{0.8}Zr_{0.2}O_{2-x}$ solid solution catalyst: a pathway to coke-resistant CO_2 reforming of methane. RSC Sustain. 2025;3:844–855.

70. Wang J, Mueller DN, Crumlin EJ. Recommended strategies for quantifying oxygen vacancies with X-ray photoelectron spectroscopy. J Eur Ceram Soc. 2024;44:116709.

71. Zhang B, Cai W, Li Y, Xu Y, Shen W. Hydrogen production by steam reforming of ethanol over an Ir/CeO_2 catalyst: reaction mechanism and stability of the catalyst. Int J Hydrog Energy. 2008;33:4377–4386.

72. Livio D, Diehm C, Donazzi A, Beretta A, Deutschmann O. Catalytic partial oxidation of ethanol over Rh/Al_2O_3: spatially resolved temperature and concentration profiles. Appl Catal A. 2013;467:530–541.

73. Chen L, Filot IAW, Hensen EJM. Elucidation of the reverse water-gas shift reaction mechanism over an isolated Ru atom on CeO_2(111). J Phys Chem C. 2023;127:20314–20325.

74. Xie L et al. Effect of oxygen vacancy influenced by CeO_2 morphology on the methanol catalytic reforming for hydrogen production. Int J Hydrog Energy. 2023;48:33119–33129.

75. Tsang S, Claridge J, Green M. Recent advances in the conversion of methane to synthesis gas. Catal Today. 1995;23:3–15.

76. Rostrupnielsen J, Hansen JB. CO_2-reforming of methane over transition metals. J Catal. 1993;144:38–49.

77. Yuan J et al. One-step dip-coating of uniform γ-Al_2O_3 layers on cordierite honeycombs and its environmental applications. Ceram Int. 2016;42:14384–14390.

78. Menon PG, Zwinkels MM, Johansson E, Jaeraes S. Monolithic honeycombs in industrial catalysis. Kinet Catal. 1998;39:615–624.

79. Boyano A et al. A comparative study of V_2O_5/AC and V_2O_5/Al_2O_3 catalysts for the selective catalytic reduction of NO by NH_3. Chem Eng J. 2009;149:173–182.

80. Araque M, Vargas JC, Zimmermann Y, Roger AC. Study of a CeZrCoRh mixed oxide for hydrogen production by ethanol steam reforming. Int J Hydrog Energy. 2011;36:1491–1502.

81. Shakor ZM, Al-Shafei EN. The mathematical catalyst deactivation models: a mini review. RSC Adv. 2023;13:22579–22592.

List of Symbols, Abbreviations, and Acronyms

CPOX	Catalytic Partial Oxidation
EDS	Energy Dispersive Spectroscopy
GC	Gas Chromatograph
GDC	Gd-Doped CeO_2
H_2-TPR	Hydrogen Temperature-Programmed Reduction
NC	Ni-CeO_2
NG	Ni-GDC
Ni	Nickel
NRC	Ni/Ru-CeO_2
NRG	Ni/Ru-GDC
Ru	Ruthenium
SEM	Scanning Electron Microscopy
XPS	X-ray Photoelectron Spectroscopy
XRD	X-ray Diffraction
TGA	Thermogravimetric Analysis
C_i	Number of Carbon Atoms in Product i
$F_{EtOH,converted}$	Molar Flow Rate of Ethanol Consumed
$F_{EtOH,in}$	Inlet Molar Flow Rates of Ethanol
$F_{EtOH,out}$	Outlet Molar Flow Rates of Ethanol
F_{H_2}	Outlet Molar Flow Rate of Hydrogen
F_i	Molar Flow Rate of Carbon-Containing Product i
X_{EtOH}	Ethanol Conversion
Y_{H_2}	H_2 Yield
$Y_{C,i}$	Carbon-Based Product Yields

1 (PDF)	DEFENSE TECHNICAL INFORMATION CTR DTIC OCA
1 (PDF)	DEVCOM ARL FCDD RLB CI TECH LIB